Journal of Physics and Chemistry of Solids 87 (2015) 259–270

Contents lists available at ScienceDirect

Journal of Physics and Chemistry of Solids

journal homepage: www.elsevier.com/locate/jpcs

Temperature dependence of dc electrical conductivity of activated carbon–metal oxide nanocomposites. Some insight into conduction mechanisms

Adrián Barroso-Bogeat [a,*], María Alexandre-Franco [a], Carmen Fernández-González [a], José Sánchez-González [b], Vicente Gómez-Serrano [a]

[a] Department of Organic and Inorganic Chemistry, Faculty of Sciences, University of Extremadura, Avda. de Elvas s/n, E-06006 Badajoz, Spain
[b] Department of Mechanical, Energetic and Materials Engineering, University of Extremadura, Avda. de Elvas s/n, E-06006 Badajoz, Spain

ARTICLE INFO

Article history:
Received 10 May 2015
Received in revised form
22 July 2015
Accepted 28 August 2015
Available online 5 September 2015

Keywords:
Microporous materials
Semiconductors
Chemical synthesis
Electrical conductivity
Electronic structure

ABSTRACT

From a commercial activated carbon (AC) and six metal oxide (Al_2O_3, Fe_2O_3, SnO_2, TiO_2, WO_3 and ZnO) precursors, two series of AC–metal oxide nanocomposites are prepared by wet impregnation, oven-drying at 120 °C, and subsequent heat treatment at 200 or 850 °C in inert atmosphere. The temperature-dependent dc electrical conductivity of AC and the as-prepared nanocomposites is measured from room temperature up to ca. 200 °C in air atmosphere by the four-probe method. The decrease in conductivity for the hybrid materials as compared to AC is the result of a complex interplay between several factors, including not only the intrinsic conductivity, crystallite size, content and chemical nature of the supported nanoparticles, which ultimately depend on the precursor and heat treatment temperature, but also the adsorption of oxygen and water from the surrounding atmosphere. The conductivity data are discussed in terms of a thermally activated process. In this regard, both AC and the prepared nanocomposites behave as semiconductors, and the temperature-dependent conductivity data have been interpreted on the basis of the classical model proposed by Mott and Davis. Because of its high content of heteroatoms, AC may be considered as a heavily doped semiconductor, so that conduction of thermally excited carriers via acceptor or donor levels is expected to be the dominant mechanism. The activation energies for the hybrid materials suggest that the supported metal oxide nanoparticles strongly modify the electronic band structure of AC by introducing new trap levels in different positions along its band gap. Furthermore, the thermally activated conduction process satisfies the Meyer–Neldel rule, which is likely connected with the shift of the Fermi level due to the introduction of the different metal oxide nanoparticles in the AC matrix.

1. Introduction

Nowadays, semiconductor metal oxides (MOs, hereafter) have received a great deal of attention and research activity, mainly due to most of them exhibit photocatalytic properties which are very useful in degradation and removal processes of organic and inorganic pollutants both in liquid and gaseous effluents [1]. Such MOs include TiO_2, Fe_2O_3, ZnO, WO_3, and SnO_2, the first being by far the most widely employed and investigated. In addition, some of these MOs are used as heterogeneous catalysts in a variety of organic reactions with industrial interest [1], as well as in solid state gas sensing devices for the detection and quantification of several toxic, environmentally hazardous, combustible or explosive gases and vapors [2,3]. Other common fields of application include gas and liquid adsorption, electronics, energy storage devices, solar cells, and so on [4]. In some of these applications, semiconductor MOs can be used either as solid phases with different particle sizes and morphologies or, most commonly in recent years, as bare nanoparticles (i.e., particles having a size in the range from 1 to 100 nm in one or more dimensions [5]) embedded or supported on a wide range of solid materials with suitable properties. Among the great variety of supports, carbon materials have been long selected because of a number of desirable characteristics. In the case of activated carbon (AC, henceforth), such properties have been the subject of several reviews [6–9].

Among other factors (specific surface area, pore size distribution, chemical and thermal stability, presence of electroactive sites, and so on), electrical conductivity largely determines the application and performance of carbon-based nanocomposites as electrode materials in energy storage devices, such as supercapacitors [10,11] and lithium

* Corresponding author. Fax: +34 924 271449.
E-mail address: adrianbogeat@unex.es (A. Barroso-Bogeat).

http://dx.doi.org/10.1016/j.jpcs.2015.08.021
0022-3697/

ion batteries [12,13]. For specific applications, especially those in automotive traction, the aforesaid energy storage systems usually have to work over a wide temperature range [14], which significantly affects their overall resistance, conductivity and capacitance. On the other hand, the working principle of semiconductor MO gas sensors relies on changes of electrical conductivity as a result of the interaction with gases and vapors in the surrounding atmosphere [15]. The magnitude of the change in conductivity, and thereby the gas response and sensitivity, are strongly dependent on the surface area, porosity, agglomeration, donor-density and acid–base properties of the MO nanoparticles, as well as on the operating temperature [3]. Moreover, it has been pointed out the existence of a correlation between the electrical conductivity of semiconductor MOs and their catalytic behavior and gas sensing properties [16]. Therefore, it becomes apparent that the study of the temperature dependence of the electrical conductivity for AC–MO nanocomposites is a key issue in order to achieve a better understanding of the involved conduction mechanisms, as well as to improve and optimize their performance as gas sensors and electrode materials in energy storage devices.

There are many studies of the electrical conductivity of AC-based materials, most of them being limited to measurements at room temperature and often focused on the adsorption characteristics of vapors and gases, such as oxygen and water, rather than on their intrinsic transport properties [17]. Based on a previous literature review, we only collected a few papers concerning the analysis of the temperature-dependent electrical conductivity in ACs prepared from different precursors both by physical and chemical activation methods [18–22]. Nevertheless, no comparative report on the electrical behavior of different AC–MO nanocomposites over a wide temperature range was found. Accordingly, there is an evident lack of knowledge about the electrical behavior of AC–MO nanocomposites under different temperatures and the electronic conduction mechanisms. In this connection, conductivity measurements are considered a powerful tool, which has been extensively applied to obtain relevant information about the electric conduction process in semiconductor materials [23,24].

Herein, the temperature dependence of the electrical conductivity is studied from room temperature up to ca. 200 °C in air atmosphere for two series of AC–MO nanocomposites, which have been previously prepared from a commercial AC and six MO (Al_2O_3, Fe_2O_3, SnO_2, TiO_2, WO_3 and ZnO) precursors by wet impregnation, oven-drying at 120 °C and subsequent heat treatment at two very different temperatures, 200 and 850 °C, in inert atmosphere [23,24]. Thus, the influence of both the MO precursor and heat treatment temperature on the conductivity and electrical behavior of the prepared nanocomposites is investigated. Obtained results are related with the electronic band structure of the raw AC and the AC–MO hybrid materials, as well as with the involved conduction mechanisms. The electrical conductivity of these nanocomposites has also been studied under moderate compression in a recent work [25].

2. Materials and methods

2.1. Materials and reagents

A granular AC purchased from Merck® (Darmstadt, Germany), 1.5 mm average particle size (Cod. 1.02514.1000), as received without any further treatment, was used as support of a broadly varied series of MOs, including Al_2O_3, Fe_2O_3, SnO_2, TiO_2, WO_3 and ZnO. The employed MO precursors were $Al(NO_3)_3 \cdot 9H_2O$, $Fe(NO_3)_3 \cdot 9H_2O$, $SnCl_2 \cdot 2H_2O$, $Na_2WO_4 \cdot 2H_2O$ and $Zn(NO_3)_2 \cdot 6H_2O$, all of them supplied by Panreac® (Barcelona, Spain) and being of reagent grade. Anatase powder from Aldrich® (Steinheim, Germany), less than 325 mesh average particle size, was also used as TiO_2 precursor.

Table 1
Methods of preparation and sample codes for AC–MO nanocomposites[a].

Series	Precursor	MHTT/°C	*t*/h	A	Code
Series 1	$Al(NO_3)_3 \cdot 9H_2O$	200	2	N_2	A200
	$Fe(NO_3)_3 \cdot 9H_2O$	200	2	N_2	F200
	$SnCl_2 \cdot 2H_2O$	200	2	N_2	S200
	TiO_2 (anatase)	200	2	N_2	T200
	$Na_2WO_4 \cdot 2H_2O$	200	2	N_2	W200
	$Zn(NO_3)_2 \cdot 6H_2O$	200	2	N_2	Z200
Series 2	$Al(NO_3)_3 \cdot 9H_2O$	850	2	N_2	A850
	$Fe(NO_3)_3 \cdot 9H_2O$	850	2	N_2	F850
	$SnCl_2 \cdot 2H_2O$	850	2	N_2	S850
	TiO_2 (anatase)	850	2	N_2	T850
	$Na_2WO_4 \cdot 2H_2O$	850	2	N_2	W850
	$Zn(NO_3)_2 \cdot 6H_2O$	850	2	N_2	Z850

[a] Abbreviations: MHTT, maximum heat treatment temperature; *t*, isothermal time at MHTT; A, atmosphere.

2.2. Preparation of the AC–MO nanocomposites

The preparation of the AC–MO nanocomposites was carried out following the methods previously described in detail by Barroso-Bogeat et al. [23,24], which are briefly summarized in Table 1 together with the codes assigned to the resulting products. Accordingly, two series of hybrid materials were prepared depending on heating conditions, named as series 1 (200 °C, 2 h) and series 2 (850 °C, 2 h). For comparison purposes, two additional samples were obtained by heating only AC, in the absence of any MO precursor, under the same conditions as in the preparation of the AC–MO nanocomposites. Such samples are referred to in the text as AC200 and AC850.

2.3. Characterization of the AC–MO nanocomposites

2.3.1. Ash content

The ash content of the hybrid materials was determined by incineration at 650 °C for about 12 h in air, using a muffle furnace (Selecta®). The soaking time at this temperature was long enough to ensure the complete oxidation and conversion of the material fraction contained in each sample into gaseous products and residual ashes. The results have been recently reported elsewhere [24,25], and are listed in Table 2.

2.3.2. X-ray diffraction (XRD)

The crystalline phases present in each nanocomposite were investigated by powder XRD, using a D8 Bruker® Advance diffractometer working with Cu Kα radiation ($\lambda = 1.5406$ Å). The identification of such phases was performed by comparing peak positions and intensities with standard JCPDS files and with data previously reported in literature. The average crystallite size (D) was estimated for each crystalline phase by applying the Scherrer equation [42] to its corresponding diffraction peak.

The powder XRD patterns registered for both series of nanocomposites are illustrated in Fig. S1. The crystalline phases identified for each hybrid material, together with their corresponding weight fraction and mean crystallite size, have been reported in a recent work [24] and are gathered in Table 2. The actual electrical conductivity of these metal phases supported on AC is very difficult to know accurately, as it strongly depends on a number of factors such as the amorphous or crystalline nature of the phase, the particle size, the presence of vacancies or dopant impurities, and so on [43]. Fortunately, the effects of these factors as a rule only modify the conductivity values of the bulk phases by less than one order of magnitude. These values are found in specialized

Table 2
Ash content, crystalline phases, and their weight fraction (W), mean crystallite size (D) and bulk electrical conductivity at room temperature (σ_{RT}), for the prepared AC–MO nanocomposites.

Sample	Ash content/wt%	Crystalline phase	W/wt%	D/nm	σ_{RT}/ S m^{-1}
A200	8.86	Alumina (Al_2O_3)	9.9	1.88	10^{-12} [26]
F200	13.55	Hematite (α-Fe_2O_3)	23.4	3.22	$4.76 \cdot 10^{-4}$ [27]
		Goethite (α-FeO(OH))	26.3	3.17	$5 \cdot 10^{-5}$ [28]
		Magnetite (Fe_3O_4)	9.6	6.19	$2.25 \cdot 10^{4}$ [29]
S200	27.21	Cassiterite (SnO_2)	16.0	4.05	$1.9 \cdot 10^{-4}$ [30]
		Romarchite (SnO)	5.0	5.07	$5.40 \cdot 10^{-4}$ [31]
T200	8.05	Anatase (TiO_2)	11.4	3.53	$6.71 \cdot 10^{-3}$ [32]
W200	9.93	Tungsten trioxide (WO_3)	4.4	2.37	$1.3 \cdot 10^{-6} - 7.5 \cdot 10^{-6}$ [33,34]
		Tungstite ($WO_3 \cdot H_2O$)	1.4	3.05	$6.7 \cdot 10^{-2}$ [35]
Z200	9.45	Zinc oxide (ZnO)	0.9	20.80	$4.8 \cdot 10^{-8} - 1.3 \cdot 10^{-6}$ [36]
		Wülfingite (ε-$Zn(OH)_2$)	7.3	1.89	$< 10^{-9}$ [37]
A850	5.68	Corundum (α-Al_2O_3)	11.0	2.06	
F850	14.66	Hematite (α-Fe_2O_3)	41.2	36.60	$4.76 \cdot 10^{-4}$ [27]
		Maghemite (γ-Fe_2O_3)	5.9	15.11	$2.85 \cdot 10^{-5}$ [38]
		Iron (Fe)	22.0		$1.0 \cdot 10^{7}$ [39]
S850	2.34	Cassiterite (SnO_2)	3.3	36.16	$1.9 \cdot 10^{-4}$ [30]
		Tin (β-Sn)	1.6	89.62	$9.9 \cdot 10^{6}$ [39]
T850	9.33	Anatase (TiO_2)	7.3	2.31	$6.71 \cdot 10^{-3}$ [32]
		Rutile (TiO_2)	7.1	1.86	$< 10^{-7}$ [40]
W850	11.54	Tungsten (W)	9.0	48.36	$1.9 \cdot 10^{7}$ [39]
		Tungsten carbide ($W_6C_{2.54}$)	7.8	3.67	$5.0 \cdot 10^{4}$ [41]
Z850	6.18	Zinc oxide (ZnO)	0.6	69.38	$4.8 \cdot 10^{-8} - 1.3 \cdot 10^{-6}$ [36]

literature and have also been included in Table 2.

2.3.3. Textural

The textural characterization of AC, AC heat-treated products and the prepared AC–MO nanocomposites was accomplished by N_2 adsorption at −196 °C and mercury porosimetry. The specific surface area (S_{BET}) was estimated by applying the Brunauer, Emmet and Teller (BET) equation [44] to the experimental N_2 adsorption isotherms measured in a semiautomatic equipment (Autosorb 1, Quantachrome®). The theoretical background for microporosity characterization was based on Dubinin's theory. Thus, the application of the Dubinin–Radushkevich (D–R) equation to the adsorption isotherms led to the values of the micropore volume (W_0) [45]. The mesopore (V_{me}) and macropore (V_{ma}) volumes were derived from the mercury intrusion curves obtained in a mercury porosimeter (PoreMaster-60, Quantachrome®). Finally, the total pore volume (V_T') was calculated from W_0, V_{me} and V_{ma}. These textural parameters for the raw AC, AC heat-treated samples, and the prepared hybrid materials have been previously reported and discussed elsewhere [23], and are collected in Table S1.

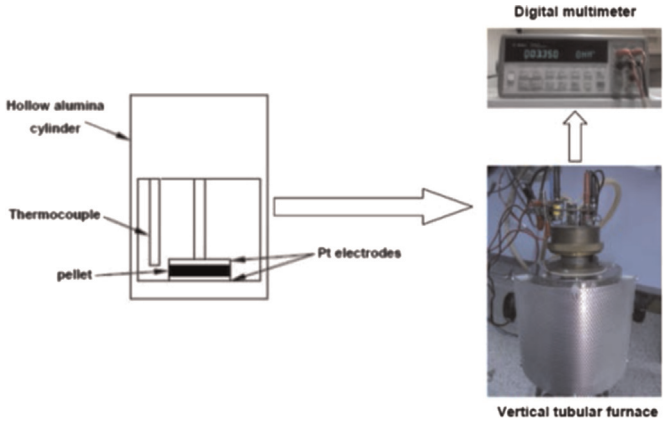

Fig. 1. Experimental device used for the measurement of the temperature-dependent dc electrical conductivity [22].

2.4. Study of temperature dependence of dc electrical conductivity

The temperature dependence of the dc electrical conductivity (σ) was studied following the simple procedure previously described in detail by our research group [22]. The AC samples and the prepared nanocomposites were compressed into circular pellets with a total mass of around 200 mg, 13.2 mm in diameter and a variable thickness ranging from 1.1 to 1.8 mm, using powder polyvinylidene fluoride (PVDF, Aldrich®, Steinheim, Germany) as binder at the 80:20 wt% sample to PVDF ratio. Prior to carrying out the electrical conductivity measurements, the pellets were stored in a desiccator to prevent the adsorption of gases and vapors from the laboratory atmosphere. As seen in Fig. 1, each pellet was placed inside a hollow alumina cylinder between two platinum foils forming the electrodes, the upper one movable and the lower one fixed, to get ohmic contact. The hollow cylinder was kept inside a vertical tubular furnace. A K-type thermocouple, whose hot junction is located close to the pellet, was used to accurately monitor the temperature during the measurements. The system was heated from room temperature up to ca. 200 °C in air atmosphere at a heating rate of 10 °C min^{-1} and, then, it was allowed to cool down to room temperature under the same atmosphere. The dc electrical resistance was registered in steps of 5 °C by the four-probe method [46], using a digital multimeter (Agilent®, model 34401A) connected to the electrodes. Such an experimental arrangement was selected in order to eliminate the resistance of the electrical contacts. Since the conduction was considered to be ohmic in nature, the electrical conductivity was given by the following expression [47]:

$$\sigma = \frac{h}{R \cdot A} \quad (1)$$

where R is the electrical resistance in Ω, A the area of the pellet surface in m^2, and h the thickness of the pellet in m. The resistance of the platinum electrodes was previously checked and found to be ~0.38 Ω, much lower than those of the samples under study.

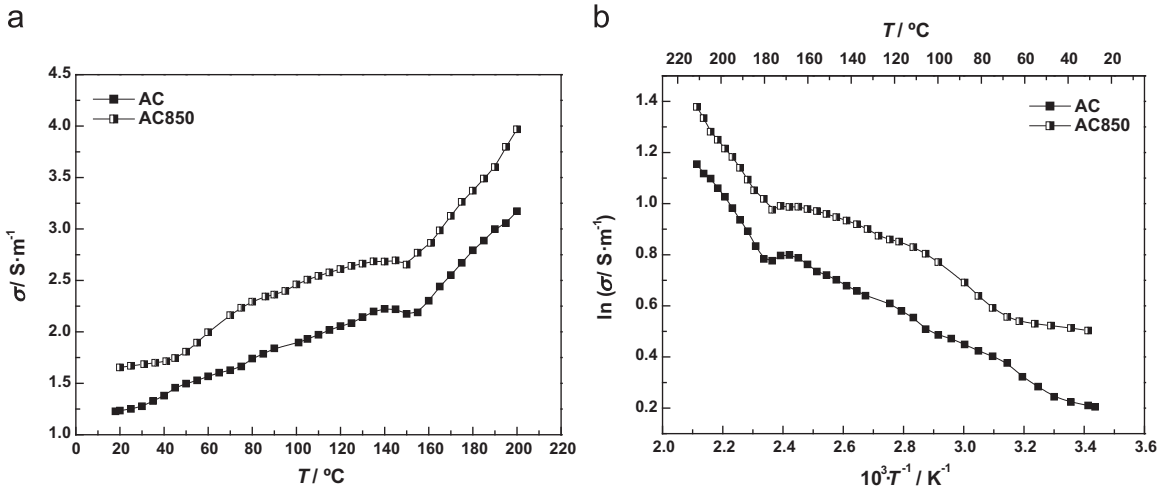

Fig. 2. Temperature dependence of the dc electrical conductivity (a) and Arrhenius-type plot of ln σ versus T^{-1} (b) for the raw AC and the heat-treated sample AC850.

3. Results and discussion

3.1. General remarks

First, it should be noted that the PVDF used as binder in the present work is supposed to be homogeneously mixed and dispersed with each nanocomposite in the pellets. This polymer has been long recognized as an excellent insulator, as inferred from its typical conductivity value in the range from 10^{-15} to 10^{-16} S m^{-1} [48]. Since the conductivity values measured for the pellets are comparatively much higher, the major contribution to their electrical conductivity is assumed to come from the nanocomposites. On the other hand, the electrical conductivity of the prepared AC–MO hybrid materials is determined by the intrinsic conductivity of their single components (i.e., supported MO nanoparticles and AC) and the resistance existing between them [49].

3.2. Temperature dependence of dc electrical conductivity for AC and AC samples

3.2.1. Bulk dc electrical conductivity

Fig. 2(a) shows the variation of the electrical conductivity with temperature for the raw AC and the sample AC850. For the sake of simplicity, the curve for the sample AC200 has been omitted in the above figure due to its great similarity to that for AC. It is seen first that electrical conductivity increases with temperature for both carbon samples, being a typical feature of semiconductor materials [50]. In addition, a slight increase of 1.2–1.4 times in the conductivity of AC is observed after heating at 850 °C in inert atmosphere for 2 h, which is likely associated with the progressive thermal decomposition of a variety of oxygen-containing surface functional groups and structures present in the raw carbon material during such heat treatment. In this connection, it should be noted that the thermal behavior of AC during its heating from room temperature up to 900 °C in inert atmosphere has been recently investigated by our research group using TG-DTG and TPD techniques. Results (see Fig. S2) clearly reveal the occurrence of various overlapped effects of mass loss attributable to the release mainly of H_2O and CO_2, and to a lesser extent of CO, coming from the hygroscopic water and the thermal decomposition of different oxygen surface functionalities, such as carboxylic acid and anhydride groups, lactones, pyrone and chromene structures, phenolic groups, ether type structures, and so on. Several previous works have proved that the electrical conductivity of carbon materials is strongly dependent on their surface chemistry [51–55] and, as a rule, this property increases with decreasing concentration of surface functional groups, especially those containing oxygen and sulfur [53]. According to Smeltzer and McIntosh [51], the formation of functional groups and structures on activated carbon surface through the reaction of oxygen with electron donating carbon atoms located on the edge of the graphene layers brings about a certain localization of the conduction electrons and, thereby, an increase in electrical resistance.

According to Hernández et al. [56] and Emmerich et al. [57], changes not only in surface chemistry but also in porosity occurring during the heat treatment should be considered in order to explain the bulk electrical conductivity of the resulting carbon products. As seen in Table S1 and previously discussed elsewhere [23], both AC and AC-derived samples are essentially microporous solids and possess a well-developed surface area ranging from 711 m^2 g^{-1} for AC to 746 m^2 g^{-1} for AC850. The raw AC exhibits a very broad pore size distribution in the three porosity regions (i.e., micro-, meso- and macroporosity), which remains practically unaltered after the heat treatments at 200 and 850 °C. The W_0 is slightly higher for AC200 and AC850 than for AC, in contrast to the microporosity decrease frequently reported for carbons heated at high temperature [58,59], while V_{me} and V_{ma} are somewhat lower for the two heat-treated AC samples. Both effects on porosity seem to balance and, as a result, V_T' is rather similar for the three carbon samples. In brief, the heat treatment of AC either at 200 or 850 °C only originates modifications of little significance in the porous texture of the material. Therefore, one infers that the contribution of the aforesaid textural changes to the magnitude of the increase in electrical conductivity of AC produced upon heat treatment at 850 °C may be considered almost negligible as compared to that attributable to the modifications in surface chemistry. In this regard, it should be borne in mind that the overall resistivity of granular and powder carbon materials is largely a function of the matter-free space in the sample. Such space comprises not only the interparticle voids but also the porosity corresponding to the intraparticle voids. As a consequence, the electrical conductivity should increase as the total pore volume decreases.

3.2.2. Electron conduction mechanism

Obviously, experimental data on electrical transport properties can only be analyzed and interpreted properly in terms of a model for the electronic structure of the carbon materials. As the dc conductivity of the samples increases with temperature, it has been considered appropriate to discuss such properties on the basis of classical models for amorphous semiconductors. The most

widely applied model is that proposed by Mott and Davis [60,61], which establishes five different conduction mechanisms: (i) variable range hopping at the Fermi level, (ii) fixed range hopping at the Fermi level, (iii) hopping in band tails, (iv) extended state conduction, and (v) conduction via donor or acceptor levels in the case of doping. All five mechanisms contribute to the experimental conductivity values. Because of the high content of heteroatoms, especially oxygen and silicon, for AC and AC850 (see Table S2), it can be assumed that these carbon samples are heavily doped or contaminated semiconductors, so that conduction of thermally excited carriers through acceptor or donor levels is expected to be by far the dominant mechanism.

It is well-known that the temperature dependence of the electrical conductivity for semiconductor materials obeys to a mechanism of thermal activation, which can be expressed by the following Arrhenius-type equation [50]:

$$\sigma = \sigma_0 \cdot \exp\left(-\frac{\Delta E}{k_B T}\right) \quad (2)$$

where ΔE is the thermal activation energy for electronic conduction or the so-called energy gap associated with electron hopping between conductive sites [62,63], k_B stands for the Boltzmann constant, T the temperature, and σ_0 refers to a constant whose value only depends on the material properties but not on the temperature [50]. It becomes evident that the factor $k_B T$ must surpass the ΔE value in order to electrical conduction takes place. The above equation can be expressed in linear form as follows:

$$\ln \sigma = \ln \sigma_0 - \frac{\Delta E}{k_B T} \quad (3)$$

Accordingly, if the material exhibits semiconductor behavior, the plot of ln σ versus T^{-1} should give a straight line, and the parameters ΔE and σ_0 may be estimated from the slope and the intercept, respectively, of the corresponding fitted line. The plots of ln σ versus T^{-1} for the samples AC and AC850 are depicted in Fig. 2(b). One observes that the plots clearly show two nearly linear portions, thus revealing that both carbon samples behave as typical extrinsic semiconductor materials [18,19]. The first linear section ranges from room temperature up to around 170–180 °C and it is related with a pure extrinsic semiconductor behavior of the samples, while the second one comprises temperatures above 170–180 °C, being associated with a pure intrinsic semiconductor behavior. These results are in very good agreement with those previously reported for other activated carbons prepared from coconut shell [18] and rice husk [19] by chemical activation with KOH and H_3PO_4, respectively. Both linear portions observed in the curves for AC and AC850 in Fig. 2(b) have been fitted to Eq. (3) and, as a result, two activation energy values have been estimated for each carbon sample. These are referred to henceforth as ΔE_1 and ΔE_2 for the lower and the upper temperature range, respectively, and the obtained values are gathered in Table 3. As can be seen, ΔE_1 and ΔE_2 remain almost unaltered after heating AC at 850 °C, thus suggesting such a heat treatment does not modify significantly the electronic band structure of the pristine carbon material. According to Fritzsche [64], the magnitude of ΔE_2 in amorphous semiconductors, such as activated carbons, is roughly half of that of the energy gap (E_g). These E_g values for both carbon samples have also been included in Table 3. One notes that they are relatively close to the band gap estimated for polycrystalline graphite (i.e., around 0.04–0.05 eV [65]), which is likely connected with a certain degree of graphitization in the raw AC as a result of both the feedstock and the experimental method followed in its preparation process. In this regard, the presence in these carbon samples of a nanocrystalline structure consisting of small domains of coherent, parallel stacking of graphene sheets with an average size of around 2.39 nm and embedded in an amorphous carbon matrix has been evidenced by powder XRD (see Fig. S3). Moreover, Mrozowski and Kmetko [65–67] demonstrated that for the whole class of aromatic solids ranging from aromatic molecular systems to perfect crystalline graphite through condensed aromatics, baked carbons, and polycrystalline graphite, the energy gap between the filled π band and the conduction band decreases steadily with increasing molecular dimensions until it disappears for large single graphite crystals. Therefore, it becomes apparent that the lower the energy gap for a given activated carbon, the greater its graphitization degree. Furthermore, it is worth noting that the slight decrease in E_g for AC850 as compared to AC (around 0.013 eV, see Table 3) may be accounted for the aforementioned thermal decomposition of oxygen surface functional groups and structures during the heat treatment of AC at 850 °C. The release of such oxygen functionalities mostly as H_2O, CO and CO_2 leads to an increase of the aromatization degree in the resulting carbon product and hence to a reduction of its band gap. On the other hand, ΔE_1 is connected with the presence not only of impurities but also of dangling bonds at point defects in the carbon matrix, which contribute to create mid gap states or levels within the band gap of the AC samples [19,60]. Indeed, it is well established that the incorporation of impurities or dopants in the structure of semiconductor materials leads to the appearance of electron donor trap levels (E_d) near the edge of the conduction band or acceptor trap levels (E_a) close to the edge of the valence band, thus lowering substantially the energy gap. In the first case, the major charge carriers are electrons and the energy barrier to form one of them is (E_g–E_d), while in the second case holes are the predominant charge carriers, being E_a the energy barrier which must be overcome to create an electronic hole. The elucidation of whether electrons or holes are the majority charge carriers involved in the conduction process requires thermopower or Hall effect measurements, which have not been included in the present work. Nevertheless, some previous works [18,68] have revealed that, for activated carbons and other amorphous carbon materials, holes and electrons are the majority charge carriers below and above 130 °C, respectively. Such a temperature is not far away from that observed for the extrinsic to intrinsic transition in samples AC and AC850 (i.e., 170–180 °C), so it allows us to suppose that holes are the predominant carriers in the region of extrinsic semiconductor behavior. From data in Table 3 it is also evident the presence of a mid gap level at 0.052 eV above the valence band or below the conduction band

Table 3
Activation energies, pre-exponential factors and energy gap estimated for AC, AC850 and prepared AC–MO nanocomposites.

Sample	ΔE_1/eV	$\sigma_{0,1}$/S m^{-1}	ΔE_2/eV	$\sigma_{0,2}$/S m^{-1}	E_g/eV	Sample	ΔE_1/eV	$\sigma_{0,1}$/S m^{-1}	ΔE_2/eV	$\sigma_{0,2}$/S m^{-1}	E_g/eV
AC	0.052	9.535	0.144	108.922	0.287	AC850	0.052	12.115	0.137	113.249	0.274
A200	0.104	25.938	0.156	99.703	0.312	A850	0.031	2.600	0.153	69.220	0.307
F200	0.021	3.920	0.229	264.805	0.458	F850	0.059	9.357	0.135	72.456	0.269
S200	0.026	2.064	0.226	693.572	0.452	S850	0.036	2.804	0.182	139.375	0.363
T200	0.036	3.881	0.198	298.792	0.397	T850	0.053	8.206	0.149	108.760	0.298
W200	0.070	7.064	0.234	606.566	0.467	W850	0.061	9.149	0.191	366.575	0.383
Z200	0.063	10.784	0.153	97.729	0.306	Z850	0.087	16.513	0.145	74.677	0.290

Table 4
Electrical conductivity of AC, AC850 and prepared AC–MO nanocomposites at two temperature values.

Sample	σ_1/S m^{-1} T=25 °C	σ_2/S m^{-1} T=200 °C	PIEC[a]	Sample	σ_1/S m^{-1} T=25 °C	σ_2/S m^{-1} T=200 °C	PIEC[a]
AC	1.251	3.172	154	AC850	1.670	3.969	138
A200	0.583	2.246	285	A850	0.783	1.634	109
F200	0.614	0.965	57	F850	0.974	2.661	173
S200	0.920	2.602	183	S850	0.787	1.606	104
T200	0.871	2.210	154	T850	1.305	2.779	113
W200	0.783	1.919	145	W850	0.923	3.231	250
Z200	0.959	2.312	141	Z850	0.789	2.142	171

[a] Percentage of increase in electrical conductivity.

both for AC and AC850. This fact clearly suggests that such energy level is associated with the same impurities, which must remain unaffected in the carbon matrix after heating the raw AC at 850 °C. Based on powder XRD and EDX analyses, the main inorganic compound detected in AC is SiO_2. Finally, it should be noted that the activation energy values estimated for these two carbon samples are in agreement with the results previously reported for other activated carbons and carbonized materials [18,19,22,52,62,63,69,70].

In addition to conduction via acceptor or donor levels, three other mechanisms also satisfy the aforesaid exponential law for the temperature-dependent conductivity expressed by Eq. (2). These are fixed range hopping, extended state conduction and thermally activated hopping in band tails [60,61]. Then, it becomes apparent that the distinction between them must be made on the basis of the values determined for activation energies and pre-exponential factors. Activation energies ranging between 0.052 and 0.137 eV are considered too high for fixed range hopping at the Fermi level, so that this conduction mechanism cannot be predominant. Similarly, an excitation in extended states can neither occur as it requires pre-exponential factors near 10^5 S m^{-1} [60,61], much greater than those estimated for AC and AC850 in the present work (see Table 3). According to Mott's theory, pre-exponential factors for thermally activated hopping in band tails are between 1 and 10^{-3} S m^{-1} [60,61], comparable in magnitude with those obtained for the two carbon samples. Therefore, conduction via thermally activated hopping in band tails should have a significant contribution to the experimental conductivity values. Moreover, it is worth noting that the conductivity data for AC and AC850 are also well fitted by the exponential law for variable range hopping (VRH) near the Fermi level [60]:

$$\sigma=\sigma_0'\cdot\exp\left(\frac{T_0}{T}\right)^{1/4} \tag{4}$$

Nevertheless, even though this conduction mechanism also contributes to the measured conductivity values, its actual contribution only can be accurately investigated and determined at very low temperatures, typically below ~30 K [72], far away from the temperature range evaluated in the present work. Furthermore, Vogel et al. [61] have suggested that the linearity of the ln $\sigma - T^{-1/4}$ plot is not necessarily explained by a VRH conduction, but it is more probably originated from a superposition of the dominant conduction mechanisms in the graphite-like and non-graphite-like regions in the heterogeneous carbon network of AC and AC850.

In addition to the aforesaid conduction mechanisms established by Mott and Davis for amorphous semiconductors, some other alternative models have been developed to explain the temperature dependence of conductivity in this kind of materials. Since AC and AC850 possess very small nanographitic domains embedded in an amorphous carbon matrix, it is rather logical to assume that the temperature-dependent conductivity follows a heteroquantum dots (HQD) model [71]. In this model, the nanocrystalline domains are considered to act as quantum dots. These nanocrystals and the amorphous matrix have different band gaps and electronic band structures, thus forming heterojunction-like structures at the interface regions. Under such assumptions, conduction occurs via a thermal-assisted tunneling process. Based on fundamentals of quantum dots and heterostructures, the HQD model leads to two different regimes for conductivity: (i) at low temperatures the activation energy (i.e., ΔE_1) is identified as the energy difference between the conduction or valence band of the nanographitic domains and the Fermi level (i.e., ~0.052 eV), and (ii) at high temperatures the activation energy (i.e., ΔE_2) increases because of the temperature effect of the electronic tunneling [71], resulting in the following relationship:

$$\Delta E_2=\Delta E_1+\frac{\epsilon_c}{4} \tag{5}$$

where ϵ_c is given by:

$$\epsilon_c=\frac{e^2}{2C} \tag{6}$$

being e the electron charge and C the junction capacitance. From the experimental data of activation energies for AC and AC850, the junction capacitance has been estimated to be $2.18\cdot10^{-19}$ F and $2.34\cdot10^{-19}$ F, respectively.

3.3. Temperature dependence of dc electrical conductivity for the AC–MO nanocomposites

3.3.1. Bulk dc electrical conductivity

Table 4 collects the values of the bulk dc electrical conductivity measured for AC, AC850 and the AC–MO nanocomposites at two temperature values, T=25 °C (σ_1) and T=200 °C (σ_2). One notes that all the samples show values of σ_1 and σ_2 falling in the range of conductivity of typical semiconductor materials, i.e. from 10^{-8} to 10^5 S m^{-1} [50]. It is also seen that both σ_1 and σ_2 are much higher for AC and AC850 than for the hybrid materials prepared at 200 and 850 °C, respectively. Furthermore, the values of conductivity at the two selected temperatures are as a rule markedly lower for the nanocomposites of series 1 as compared to their respective counterparts prepared at 850 °C, except for the pairs S200–S850 and Z200–Z850. For samples of series 1, conductivity at room temperature (i.e., σ_1) varies in the order AC > Z200 > S200 > T200 > W200 > F200 > A200, while at 200 °C (i.e., σ_2) it does by AC > S200 > Z200 > A200 > T200 > W200 > F200. By contrast, for samples of series 2 the order of the variation of conductivity is AC850 > T850 > F850 > W850 > Z850 ≈ S850 ≈ A850 for σ_1, and AC850 > W850 > T850 > F850 > Z850 > A850 > S850 for σ_2. Table 4 also lists the percentage of increase in electrical conductivity (PIEC), defined as follows:

$$PIEC=\frac{(\sigma_2-\sigma_1)}{\sigma_1}\cdot100 \tag{7}$$

The value of PIEC is high for A200 and W850 and low for F200, with the rest of the AC–MO nanocomposites presenting intermediate values.

Figs. 3(a) and 4(a) show the variation of conductivity with temperature for the hybrid materials prepared by heat treatment at 200 and 850 °C, respectively. The plots for the pristine AC and the sample AC850 have also been included in the above figures for comparison purposes. From these figures, it follows that nanocomposites of series 1 and 2 also behave as semiconductor materials as their electrical conductivities increase with temperature. For samples prepared by heating at 200 °C, conductivity roughly varies in the order: AC > Z200 > T200 > A200 > S200 > W200 > F200 over a wide temperature range, while for those of series 2 conductivity is higher as

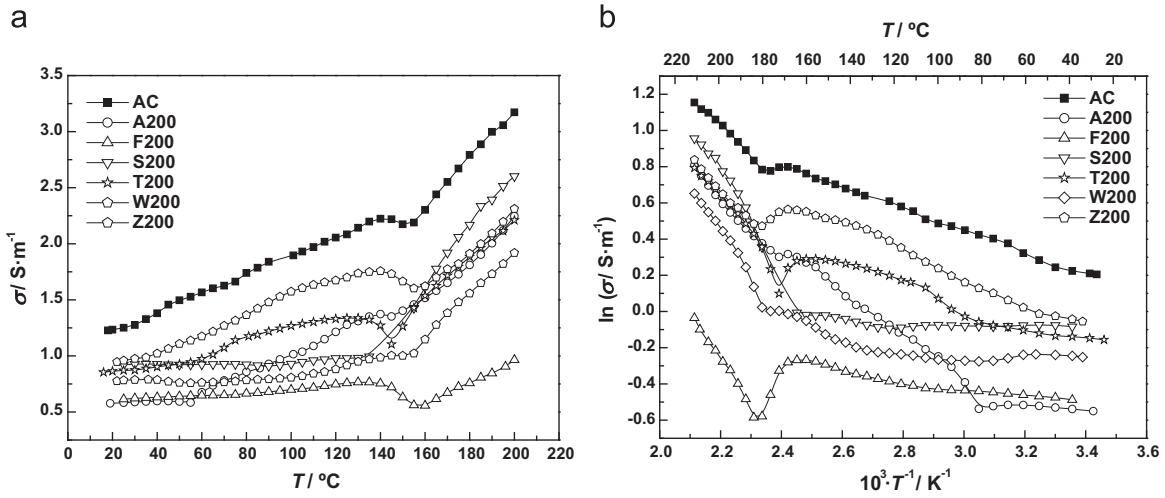

Fig. 3. Temperature dependence of the dc electrical conductivity (a) and Arrhenius-type plot of ln σ versus T^{-1} (b) for nanocomposites of series 1.

follows: AC850 > T850 > F850 > W850 > Z850 > A850 ≈ S850.

It has been recently reported that the bulk electrical conductivity of the prepared AC–MO nanocomposites is the result of a complex interplay between several factors, including the texture and the intrinsic conductivity, crystallite size, content and chemical nature of the supported nanoparticles, which ultimately depend on the MO precursor and heat treatment temperature [25]. In addition to these factors, the adsorption of oxygen and water from the surrounding atmosphere also plays a major role on the electrical properties of the hybrid materials, as seen below. An attempt of explaining the trends observed for the bulk conductivity of the nanocomposites within each series and between them on the basis of the influence of the aforementioned factors is exposed in the following paragraphs.

As far as texture is concerned, data in Table S1 clearly reveal that the preparation of AC–MO nanocomposites by wet impregnation of AC with the MO precursors, oven-drying at 120 °C, and subsequent heat treatment at 200 °C in inert atmosphere, leads to a decrease in the three porosity regions, i.e. micro-, meso- and macroporosity, for the resulting products as compared to the raw AC [23,25]. Since, as stated above, the pores in the samples act as electrical resistances, it is evident that bulk conductivity should increase with the decrease in porosity and, thereby, in total intraparticle void space (i.e., V_T'). Nevertheless, unlike the behavior observed for other porous carbon materials, the overall reduction in porosity for 200 °C nanocomposites does not result in an improvement of the electrical conductivity of AC, in view that all these hybrid materials exhibit conductivity values lower than the carbon support over the entire temperature range (see Table 4 and Fig. 3(a)). Therefore, it becomes apparent that some porosity of AC is filled and blocked by a variety of nanoparticles having a much lower conductivity than the carbon substrate itself. As seen in Table 2, such nanoparticles are mostly metal oxides (Al_2O_3, α-Fe_2O_3, Fe_3O_4, SnO_2, SnO, TiO_2-anatase, WO_3, and ZnO), accompanied in some cases by hydroxides and oxyhydroxides (α-FeO(OH) and ε-$Zn(OH)_2$), whose intrinsic electrical conductivity values are as a rule several orders of magnitude lower than those registered for the pristine AC over the investigated temperature range. As a guide, bulk electrical conductivity values at room temperature for the supported nanoparticles have also been included in Table 2. In this connection, the bulk conductivity of the hybrid materials prepared at 200 °C should decrease with increasing the content of nanoparticles and, hence, with the ash content, since it can be reasonably assumed that the greater the latter, the larger the amount of nanoparticles supported on AC. According to data in Table 2, the ash content increases in the following order: T200 < A200 < Z200 < W200 < F200 < S200, which is not correlated with conductivity. The divergence between both variation sequences for conductivity and ash content is likely attributable to the very different intrinsic conductivity of the

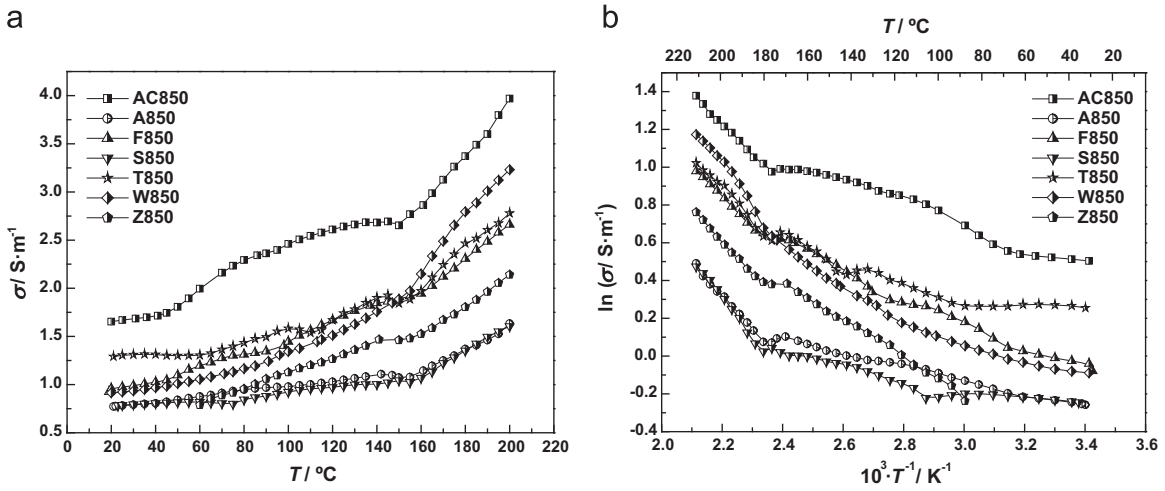

Fig. 4. Temperature dependence of the dc electrical conductivity (a) and Arrhenius-type plot of ln σ versus T^{-1} (b) for nanocomposites of series 2.

supported nanoparticles. Thus, the relatively low conductivity of A200 over the whole temperature range is justified by the well-known insulating character of the supported alumina [26], even though this sample should theoretically show a higher conductivity owing to its low ash content. Similarly, the highest ash content for S200 should give the poorest conductivity for this nanocomposite. Strikingly, one observes in Fig. 3(a) that the σ–T curve for S200 is situated above than that of F200. This fact can be accounted for by the much greater electrical conductivity of cassiterite (SnO_2) and romarchite (SnO) as compared to hematite (α-Fe_2O_3) and goethite (α-FeO(OH)), which are the main crystalline phases identified in the samples S200 and F200 (see Table 2).

By comparing data in Table 4 and the plots in Figs. 3(a) and 4(a), it becomes apparent that the rise of heat treatment temperature from 200 to 850 °C causes an improvement of conductivity for the resulting hybrid materials. As an exception to the rule, conductivity only decreases for samples S850 and Z850. However, it should be noted that the conductivities for samples of series 2 are still lower than those registered for AC850 and even for the raw AC over the investigated temperature range. This overall increase in conductivity may be explained by taking into account both composition and microstructural changes occurring in the carbon phase and the supported nanoparticles as a result of the heat treatment at 850 °C and with influence on electrical conductivity of the resulting hybrid materials. First, carbothermic reductions of MOs have been reported to occur during the heat treatment in inert atmosphere at a temperature as high as 850 °C [24]. As seen in Table 2, these reactions lead to the formation of metals in elemental state, mainly Fe, Sn and W, and even of some metal carbides, such as $W_6C_{2.54}$. Since the intrinsic conductivity of these metals and metal carbides is many orders of magnitude greater than for the corresponding MOs (see Table 2 again), their presence in the nanocomposites, even in small amounts, lowers the resistivity and brings about a significant enhancement in electrical conductivity. Second, from data in Table 2 and powder XRD patterns in Fig. S1 one observes that the heat treatment at 850 °C usually results in a development of crystallinity and in an increase of the mean crystallite size for the supported nanoparticles, irrespective of the MO precursor. This fact also redounds in the better conductivity exhibited by the 850 °C nanocomposites since, as previously shown by several works concerning the dependence of electrical properties on crystallite size for nanoparticles of metals [72] and metal oxides [73–75], the larger the crystallite size, the smaller the width of the insulating grain boundary and, hence, the greater the electrical conductivity. Furthermore, from Figs. 3(a) and 4(a) one infers that the presence of zero-valent metal nanoparticles appears to be a stronger factor than the increase of the mean crystallite size on the improvement of conductivity observed for the hybrid materials with increasing heat treatment temperature. In fact, the increase in conductivity is noticeably greater for samples F850 and W850, which contain metals in elemental state, while such an increase is less pronounced for the rest of the nanocomposites. On the other hand, by heat treatment at 850 °C porosity develops for all hybrid materials as compared to their counterparts prepared at 200 °C, the increase being more marked in the microporosity region (see Table S1). Such a porosity development entails an increase in the total intraparticle void space, which should have a detrimental effect on the conductivity of the nanocomposites of series 2. Nonetheless, conductivity improves for these hybrid materials, thus suggesting that their electrical properties are largely controlled by the chemical nature and size of the supported nanoparticles rather than by the porosity.

Oxygen-containing functional groups and structures on AC surface are involved in the adsorption of the different MO precursors from aqueous medium during the wet impregnation step [37], resulting in the formation of interface bonds between the inorganic and carbon phase. Subsequently, the inorganic phases undergo further conversions through complex chemical reactions (condensation, dehydration, dehydroxylation, etc.) during the oven-drying and heat treatment at 200 and 850 °C, leading to the formation of additional chemical bonds between the MO nanoparticles and AC. According to Torquato et al. [49], such interface bonds strongly affect the electrical properties of the resulting nanocomposites. Indeed, these bonds seem to increase the resistance between the nanoparticles and the AC support, thus decreasing the bulk conductivity of the hybrid materials.

3.3.1.1. Influence of the adsorption of oxygen and water from the surrounding atmosphere. The surrounding atmosphere has also been recognized as a major factor with influence on the electrical properties of MOs. In the present work the conductivity measurements were performed in air atmosphere, and two competitive processes involving active sites on the surface of MOs nanoparticles are known to take place under such an environment: (i) oxygen adsorption, and (ii) water adsorption [76,77]. Concerning the first one, it has been reported that the conductivity of MOs is partly influenced by chemical transformations of oxygen molecules adsorbed on catalytically active sites of the oxide surface, including the formation of O^-, O^{2-} and O_2^- chemisorbed anions. According to Vol'kenstein's theory [78], oxygen molecules chemisorb on MO surface through the formation of acceptor bonds both with metal and oxygen atoms of the lattice, the first type being stronger than the second one. The aforesaid negatively charged oxygen species are formed by the following reduction reactions [2]:

$$O_2(ad) + e^- \leftrightarrow O_2^-(ad) \quad (8)$$

$$O_2^-(ad) + e^- \leftrightarrow 2O^-(ad) \quad (9)$$

$$O^-(ad) + e^- \leftrightarrow O^{2-}(ad) \quad (10)$$

Chemisorbed oxygen ions lead to the appearance of acceptor energy levels and, as a consequence, to a promotion of electrons from the conduction band and donor states in the bulk MO [2,76], thus decreasing its electrical conductivity. In stark contrast, the adsorption of water may give rise to an increase in conductivity, probably owing to the dissociation of water molecules on the MO surface to provide protons (H^+) and hydroxyl groups (OH^-) [2,76,79]. Protons are able to bind to surface lattice oxygen atoms according to this reaction [2]:

$$H^+ + O(lat) \leftrightarrow [OH]^+ \quad (11)$$

while hydroxyl groups are bonded to lattice metal atoms by the following reaction:

$$OH^- + M(lat) \leftrightarrow [M - OH] + e^- \quad (12)$$

where M stands for a lattice metal atom. The latter process supplies a significant amount of free charge carriers, which contribute to increase the electrical conductivity of the MO.

As seen in Fig. 3(a), the σ–T curves registered for nanocomposites F200, T200 and Z200 show a narrow temperature range with decreasing conductivity, thus suggesting that oxygen is chemisorbed on MO nanoparticles and undergoes the aforesaid reduction reactions (see Eq. (8)–(10)) during the heating experiments. This conclusion is in line with the results obtained in a few previous works concerning the temperature dependence of electrical conductivity in air for pure α-Fe_2O_3, TiO_2 and ZnO prepared by several techniques and with different morphologies and particle sizes [2,76,80–82]. Nevertheless, it should be noted that the supporting of nanoparticles of these three MOs on AC surface

markedly shifts the temperature range in which the formation of chemisorbed oxygen species and the consequent drop of conductivity occur, as compared to the results reported for the pure MOs. As an illustrative example, the conductivity of pure TiO_2-anatase nanoplates was found to decrease between 30 and 100 °C [76], whereas such interval shifts upward for the nanocomposite T200, appearing from 130 to 145 °C. Furthermore, the largest decrease in conductivity with temperature is registered for sample F200, being lower for T200 and Z200, which is likely related to the MO content of each hybrid material. Thus, the higher the amount of MO, the greater the number of surface active sites for oxygen chemisorption, and the larger the decrease in conductivity. Conversely, chemisorption of water appears to predominate for nanocomposites A200, S200 and W200, since no decrease in conductivity with temperature is observed from their corresponding σ–T plots (see Fig. 3(a)). The latter assertion is also corroborated by a number of experimental data. For example, a low affinity for oxygen chemisorption and, instead, a preference towards water adsorption, has been reported for polycrystalline SnO_2 catalysts up to temperatures of 320–340 °C [83]. In addition, the formation of O^- and O^{2-} chemisorbed species on pure SnO_2 powder has been found to reach a maximum at about 200 and 600 °C [16], respectively, temperatures higher than those investigated in the present work. In the same way, water adsorption on WO_3 thin films easily occurs in air atmosphere, increasing their electrical conductivities as compared to those measured in vacuum [84], while the strong affinity of porous Al_2O_3 towards moisture has been long exploited in the preparation of humidity sensors [85].

The effect of air atmosphere on the electrical conductivity of 850 °C nanocomposites is much weaker than for those prepared at 200 °C. Thus, the narrow temperature range with decreasing conductivity is not observed in the plots of F850 and Z850, probably due to the lower MO content for these samples as compared to F200 and Z200, respectively. By contrast, from Fig. 4(a) it is seen that the σ–T plot for T850 shows two slight decreases centered at around 110 and 150 °C, which are likely attributable to oxygen chemisorption on active sites belonging to two different TiO_2 phases, i.e. anatase and rutile. In this regard, it is worth noting that rutile originates from anatase by means of a phase transition occurring in the temperature range from 600 to 700 °C for TiO_2-carbon hybrid materials [86]. According to the results obtained for T200, the drop in conductivity at 150 °C is ascribed to oxygen chemisorption on anatase, while the decrease centered at 110 °C may be related with oxygen chemisorption on the polymorph rutile.

3.3.2. Electron conduction mechanism

The plots of ln σ against T^{-1} for nanocomposites of series 1 are illustrated in Fig. 3(b), together with that for the carbon substrate. Similarly to AC and AC850, these hybrid materials also behave as extrinsic semiconductors. The activation energies (i.e., ΔE_1 and ΔE_2) estimated for these nanocomposites are also listed in Table 3. One observes from this table that the variety of nanoparticles supported on AC after wet impregnation, oven-drying at 120 °C and heat treatment at 200 °C cause significant changes not only in the magnitude of the conductivity (as seen from Table 4 and Fig. 3(a)) but also in the activation energies associated with electron conduction. These modifications may be explained if the supported nanoparticles are considered to act as impurities or dopants in the carbon matrix, introducing new trap levels in the gap of AC and thereby strongly modifying its electronic band structure. From Table 3 it follows that ΔE_2 is as a rule much higher than ΔE_1 for each nanocomposite, as expected from the extrinsic semiconductor behavior observed for such hybrid materials. As far as the high temperature linear portion of the ln σ–T^{-1} curves is concerned, ΔE_2 and hence E_g are higher for the 200 °C samples as compared to those values estimated for the raw AC, irrespective of the MO precursor. Thus, E_g increases from 0.287 eV for AC to 0.467 eV for W200 and by the following order: AC < Z200 < A200«T200«S200 < F200 < W200, being the effect stronger for W200, F200, S200 and T200, and much weaker for Z200 and A200. Therefore, it is evident that the supporting of the different MOs leads to a widening of the band gap of AC, an effect which is likely related with the formation during the preparation of chemical bonds involving the MO precursor and the oxygen-containing functional groups and structures on the surface of the carbon substrate. Such interface bonds may act as withdrawing electron groups on the aromatic rings of the basal planes in AC by means of inductive effects, thus increasing the localization of the conduction π electrons and thereby the band gap. Regarding the low temperature portion of the ln σ–T^{-1} curves, nanocomposites of series 1 can be divided into two groups depending on the effect of the supported nanoparticles on the ΔE_1 value of AC and, hence, on the position of the mid gap levels. The first group includes the samples F200, S200 and T200, whose estimated ΔE_1 values are noticeably lower than for AC and vary in the range from 0.021 eV for F200 to 0.036 eV for T200. This fact is likely connected with the insertion of new energy levels in the middle of the AC band gap due to the supported nanoparticles, which are mainly α-Fe_2O_3, α-FeO(OH), SnO_2, SnO, and TiO_2-anatase for the aforesaid nanocomposites. These mid gap levels may be either donor trap levels near the edge of the conduction band or acceptor trap levels located close to the edge of the valence band, in both cases lowering the energy gap E_g. Such a reduction may be considered as the ultimate cause responsible for the enhanced photocatalytic performance, as well as for the shift of the optical absorption edge from UV towards the visible region, recently reported for this kind of activated carbon–MO hybrid materials [87–90]. By contrast, ΔE_1 values for samples A200, W200 and Z200 are significantly greater than for AC, which suggests the insertion of acceptor or donor trap levels associated with the supported phases (i.e., mainly Al_2O_3, WO_3 and ZnO) and located in the middle of the gap above the mid gap state observed for the pristine carbon support.

Fig. 4(b) shows the temperature-dependent electrical conductivity as an Arrhenius type plot for nanocomposites of series 2, as well as for the sample AC850. As can be seen, these hybrid materials also exhibit typical extrinsic semiconductor behavior. The activation energies estimated for these samples are also collected in Table 3. From data in this table, it follows that the rise of heat treatment temperature from 200 to 850 °C leads to a narrowing of the band gap for all samples. As an example, E_g decreases from 0.458 eV for F200 to 0.269 eV for F850. Such a narrowing seems to be intimately related to the chemical nature of the supported nanoparticles, being more pronounced for those nanocomposites containing metals in the elemental state, i.e. F850, S850 and W850, whose band gaps are reduced by 0.19, 0.09 and 0.08 eV, respectively. By contrast, the contraction of E_g is almost negligible in the case of A850, probably due to the supported Al_2O_3 does not differ significantly in crystallinity and particle size from that obtained by heat treatment at 200 °C (see Table 2 and Fig. S1). Furthermore, the calcination at 850 °C results in a modification not only of ΔE_2 and E_g but also of ΔE_1 as compared to the 200 °C nanocomposites. Thus, ΔE_1 increases for samples F850, S850, T850 and Z850, while the opposite applies to A850 and W850. Again, these results are consistent with the appearance of energy levels in the middle of the AC band gap and associated with the supported nanoparticles. As expected, the position of these new energy levels differs from those in nanocomposites of series 1 in view of the differences in the chemical nature, content, crystallinity and size of the nanoparticles supported on AC as a result of the heat treatments at 200 and 850 °C.

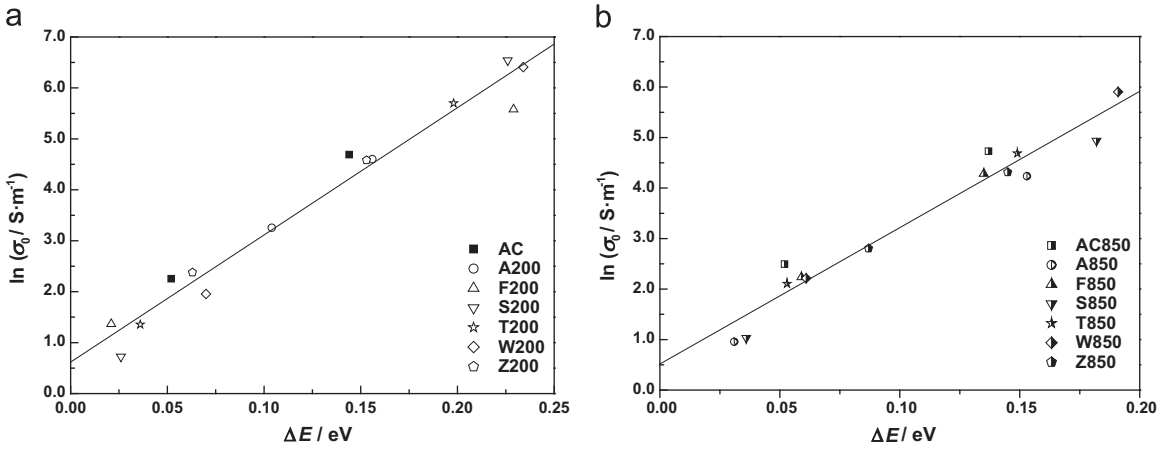

Fig. 5. The Meyer–Neldel plots of ln σ_0 versus ΔE for nanocomposites of series 1 (a) and 2 (b). The solid lines are least-squares fits.

On the other hand, the analysis of the pre-exponential factor (σ_0) also provides relevant information concerning the electron transport mechanism. As can be seen from Table 3, the pre-exponential factors estimated for samples of series 1 and 2 are remarkably lower than 10^3 S m^{-1}, thus corroborating the dominant conduction mechanism in these nanocomposites involves the thermally activated hopping of charge carriers between localized energy states along the band gap [60]. Furthermore, for a variety of materials including amorphous semiconductors a correlation between the activation energy and the pre-exponential factor has been found. This is the so-called Meyer–Neldel rule or compensation law, which can be expressed as follows [91]:

$$\sigma_0 = \sigma_{MN}\cdot\exp\left(\frac{\Delta E}{k_B\cdot T_{MN}}\right) \quad (13)$$

where T_{MN} denotes a temperature value at which the dependence of σ_0 on ΔE disappears, i.e. the Meyer–Neldel characteristic temperature. The explanation of such a behavior and its ubiquity is still open to question, although it has been recently associated with the statistical shift of the Fermi level within the band gap with a certain density of states distribution [71]. As shown in Fig. 5 (a), the dependence of ln σ_0 on ΔE proves to be linear, which confirms the validity of the compensation law for the semiconductor nanocomposites prepared by heat treatment at 200 °C. The slope of the fitted line in the above figure is 24.97 eV^{-1}, which leads to a T_{MN} value of ~465 K. Considering an electronic bulk effect, the validity of the Meyer–Neldel rule in these hybrid materials may be related to a shift of the Fermi level as a result of the introduction of the different MOs in the AC matrix. Similarly, from Fig. 5(b) it follows that the samples prepared at 850 °C also obey to the Meyer–Neldel rule with a slope for the fitted line of 26.99 eV^{-1} and a T_{MN} value of ~430 K.

4. Conclusions

Two series of AC–MO (Al_2O_3, Fe_2O_3, SnO_2, TiO_2, WO_3, ZnO) nanocomposites were prepared by wet impregnation, oven-drying at 120 °C, and subsequent heat treatment at 200 or 850 °C in inert atmosphere. The dc electrical conductivity of AC and the resulting hybrid materials was measured from room temperature up to ca. 200 °C in air atmosphere by the four-probe method. Bulk electrical conductivity is lower for the prepared nanocomposites as compared to the raw AC over the entire temperature range, and its magnitude depends on a complex interplay of several factors. Among them, the intrinsic conductivity, mean crystallite size, content and chemical nature of the supported nanoparticles, which are ultimately determined by the MO precursor and heat treatment temperature, seem to be the more relevant. Furthermore, the adsorption of oxygen and water from the surrounding atmosphere also plays a pivotal role. For each MO precursor, conductivity is found to improve with the rise of the heat treatment temperature, likely due to the increase in the crystallite size and, in some cases, to the formation of metals in elemental state and even metal carbides. The analysis of the temperature-dependent electrical conductivity measurements in terms of a thermally activated process reveals that both AC and the prepared nanocomposites behave as typical extrinsic semiconductor materials, irrespective of the MO precursor and heat treatment temperature. Therefore, the electrical conduction process is interpreted on the basis of the different mechanisms proposed by Mott and Davis for amorphous semiconductors. According to the values estimated for the activation energies and pre-exponential factors, conduction of thermally activated carriers through acceptor or donor levels is considered to be the dominant electrical transport mechanism for all samples. Furthermore, the activation energies for the hybrid materials suggest that the supported MO nanoparticles strongly modify the electronic band structure of AC by introducing new trap levels along its band gap. The position of these trap levels also depends on the crystallinity, mean crystallite size, content and chemical nature of the supported nanoparticles. The thermally activated conduction process is found to satisfy the Meyer–Neldel rule, a behavior which has been connected with a shift of the Fermi level as a result of the introduction of the different MOs in the AC matrix.

Acknowledgments

Financial support by Gobierno de Extremadura and European FEDER Funds (GR10119) is gratefully acknowledged. A. Barroso-Bogeat thanks Spanish Ministerio de Educación, Cultura y Deporte for the concession of a FPU Grant (AP2010-2574).

Appendix A. Supplementary material

Supplementary data associated with this article can be found in the online version at 10.1016/j.jpcs.2015.08.021.

References

[1] A. Barroso-Bogeat, C. Fernández-González, M. Alexandre-Franco, V. Gómez-Serrano, Activated carbon as a metal oxide support: a review, in: J.

F. Kwiatkowski (Ed.), Activated Carbon: Classifications, Properties and Applications, Nova Science Publishers, New York, 2011, pp. 297–318.
[2] X.Q. Liu, S.W. Tao, Y.S. Shen, Preparation and characterization of nanocrystalline α-Fe_2O_3 by a sol–gel process, Sens. Actuators B 40 (1997) 161–165.
[3] K. Wetchakun, T. Samerjai, N. Tamaekong, C. Liewhiran, C. Siriwong, V. Kruefu, A. Wisitsoraat, A. Tuantranont, S. Phanichphant, Semiconducting metal oxides as sensors for environmentally hazardous gases, Sens. Actuators B 160 (2011) 580–591.
[4] V. Ranjithkumar, S. Sangeetha, S. Vairam, Synthesis of magnetic activated carbon/α-Fe_2O_3 nanocomposite and its application in the removal of acid yellow 17 dye from water, J. Hazard. Mater. 273 (2014) 127–135.
[5] M.J. Iqbal, N. Yaqub, B. Sepiol, B. Ismail, A study of the influence of crystallite size on the electrical and magnetic properties of $CuFe_2O_4$, Mater. Res. Bull. 46 (2011) 1837–1842.
[6] F. Rodríguez-Reinoso, The role of carbon materials in heterogeneous catalysis, Carbon 36 (1998) 159–175.
[7] H. Marsh, F. Rodríguez-Reinoso, Activated Carbon, Elsevier, Amsterdam, 2006.
[8] F. Rodríguez-Reinoso, S. Sepúlveda-Escribano, Carbon as catalyst support, in: P. Serp, J.L. Figueiredo (Eds.), Carbon Materials for Catalysis, John Wiley & Sons, Hoboken, NJ, 2009, pp. 131–156.
[9] Y. Yang, K. Chiang, N. Burke, Porous-carbon supported catalysts for energy and environmental applications: a short review, Catal. Today 178 (2011) 197–205.
[10] L. Wei, G. Yushin, Nanostructured activated carbons from natural precursors for electrical double layer capacitors, Nano Energy 1 (2012) 552–565.
[11] M. Zhi, C. Xiang, J. Li, M. Li, N. Wu, Nanostructured carbon–metal oxide composite electrodes for supercapacitors: a review, Nanoscale 5 (2013) 72–88.
[12] Y.P. Wu, E. Rahm, R. Holze, Carbon anode materials for lithium ion batteries, J. Power Sour. 114 (2003) 228–236.
[13] S. Goriparti, E. Miele, F. De Angelis, E. Di Fabrizio, R.P. Zaccaria, C. Capligia, Review on recent progress of nanostructured anode materials for Li-ion batteries, J. Power Sour. 257 (2014) 421–433.
[14] P. Liu, M. Verbrugge, S. Soukiazian, Influence of temperature and electrolyte on the performance of activated-carbon supercapacitors, J. Power Sour. 156 (2006) 712–718.
[15] E. Comini, Metal oxide nano-crystals for gas sensing, Anal Chim. Acta 568 (2006) 28–40.
[16] V.V. Malyshev, Conductivity of semiconducting tin dioxide in dry air caused by oxygen chemical transformations and chemisorption, Russ. J. Phys. Chem. A 83 (2009) 1940–1945.
[17] A.W.P. Fung, A.M. Rao, K. Kuriyama, M.S. Dresselhaus, G. Dresselhaus, M. Endo, N. Shindo, Raman scattering and electrical conductivity in highly disordered activated carbon fibers, J. Mater. Res. 8 (1993) 489–500.
[18] W.M. Daud, M. Badri, H. Mansor, Possible conduction mechanisms in coconut-shell activated carbon, J. Appl. Phys. 67 (1990) 1915–1917.
[19] L. John Kennedy, J. Judith Vijaya, G. Sekaran, Electrical conductivity study of porous carbon composite derived from rice husk, Mater. Chem. Phys. 91 (2005) 471–476.
[20] E. Pollak, I. Genish, G. Salitra, A. Soffer, L. Klein, D. Aurbach, The dependence of the electronic conductivity of carbon molecular sieve electrodes on their charging states, J. Phys. Chem. B 110 (2006) 7443–7448.
[21] A. Subrenat, J.N. Baléo, P. Le Cloirec, P.E. Blanc, Electrical behavior of activated carbon cloth heated by the joule effect: desorption application, Carbon 39 (2001) 707–716.
[22] A. Barroso-Bogeat, M. Alexandre-Franco, C. Fernández-González, A. Macías-García, V. Gómez-Serrano, Temperature dependence of the electrical conductivity of activated carbon prepared from vine shoots by physical and chemical activation methods, Microporous Mesoporous Mater. 209 (2015) 90–98.
[23] A. Barroso-Bogeat, M. Alexandre-Franco, C. Fernández-González, V. Gómez-Serrano, Preparation of activated carbon–metal oxide hybrid catalysts: textural characterization, Fuel Process. Technol. 126 (2014) 95–103.
[24] A. Barroso-Bogeat, M. Alexandre-Franco, C. Fernández-González, V. Gómez-Serrano, Preparation and microstructural characterization of activated carbon–metal oxide hybrid catalysts: new insights into reaction paths, J. Mater. Sci. Technol. 31 (2015) 806–814, http://dx.doi.org/10.1016/j.jmst.2015.06.004.
[25] A. Barroso-Bogeat, M. Alexandre-Franco, C. Fernández-González, A. Macías-García, V. Gómez-Serrano, Electrical conductivity of activated carbon–metal oxide nanocomposites under compression. A comparison study, Phys. Chem. Chem. Phys. 16 (2014) 25161–25175.
[26] W.T. Li, D.R. McKenzie, W.D. McFall, Q.Ch Zhang, W. Wiszniewski, Breakdown mechanism of Al_2O_3 based metal-to-metal antifuses, Solid-State Electron. 44 (2000) 1557–1562.
[27] A.A. Akl, Microstructure and electrical properties of iron oxide thin films deposited by spray pyrolysis, Appl. Surf. Sci. 221 (2004) 319–329.
[28] N. Guskos, G.J. Papadopoulos, V. Likodimos, S. Patapis, D. Yarmis, A. Przepiera, K. Przepiera, J. Majszczyk, Photoacoustic, EPR and electrical conductivity investigations of three synthetic mineral pigments: hematite, goethite and magnetite, Mater. Res. Bull. 37 (2002) 1051–1061.
[29] D. Reisinger, P. Majewski, M. Opel, L. Alff, R. Gross, Hall effect, magnetization, and conductivity of Fe_3O_4 epitaxial thin films, Appl. Phys. Lett. 85 (2004) 4980.
[30] A.V. Moholkar, S.M. Pawar, K.Y. Rajpure, C.H. Bhosale, J.H. Kim, Effect of fluorine doping on highly transparent conductive spray deposited nanocrystalline tin oxide thin films, Appl. Surf. Sci. 255 (2009) 9358–9364.
[31] K. Krishnakumar, N. Pinna, K. Perumal, R. Jayaprakash, Preparation and characterization of SnO nanoplatelets by microwave innovative technique, AIP Conf. Proc. 1004 (2008) 122–125.
[32] K.W. Vogt, P.A. Kohl, W.B. Carter, R.A. Bell, L.A. Bottomley, Characterization of thin titanium oxide adhesion layers on gold: resistivity, morphology, and composition, Surf. Sci. 301 (1994) 203–213.
[33] M.G. Hutchins, O. Abu-Alkhair, M.M. El-Nahass, K. Abdel-Hady, Electrical conductivity and dielectric relaxation in non-crystalline films of tungsten trioxide, J. Non-Cryst. Solids 353 (2007) 4137–4142.
[34] M.M. El-Nahass, H.A.M. Ali, M. Saadeldin, M. Zaghllol, AC conductivity and dielectric properties of bulk tungsten trioxide (WO_3), Physica B 407 (2012) 4453–4457.
[35] L. Beluze, J.C. Badot, R. Weil, V. Lucas, Broadband dielectric and resistivity spectroscopy of $WO_3 \cdot H_2O$ in the range of 103–1010 Hz: Particle size effect, J. Phys. Chem. B 110 (2006) 7304–7308.
[36] H. Wang, C. Li, H. Zhao, R. Li, J. Liu, Synthesis, characterization, and electrical conductivity of ZnO with different morphologies, Powder Technol. 239 (2013) 266–271.
[37] M. Seredych, O. Mabayoje, M.M. Koleśnik, V. Krstić, T.J. Bandosz, Zinc (hydr) oxide/graphite based-phase composites: effects of the carbonaceous phase on surface properties and enhancement in electrical conductivity, J. Mater. Chem. 22 (2012) 7970–7978.
[38] F.G. de Souza Jr., J.A. Marins, J.C. Pinto, G.E. de Oliveira, C.M. Rodrigues, L.M.T. R. Lima, Magnetic field sensor based on a maghemite/polyaniline hybrid material, J. Mater. Sci. 45 (2010) 5012–5021.
[39] E.A. Brandes, G.B. Brook (Eds.), Smithells Metals Reference Book, 7th ed.,Butterworth Heinemann, Oxford, 1992.
[40] Th Dittrich, J. Weidmann, F. Koch, I. Uhlendorf, I. Lauermann, Temperature- and oxygen partial pressure-dependent electrical conductivity in nanoporous rutile and anatase, Appl. Phys. Lett. 75 (1999) 3980–3982.
[41] H.O. Pierson, Handbook of Chemical Vapour Deposition (CVD): Principles, Technology, and Applications, 2nd ed., William Andrew Inc., New York, 1999.
[42] B.D. Cullity, Elements of X-ray diffraction, Addison-Wesley, Reading, MA, 1959.
[43] N. Tsuda, K. Nasu, A. Fujimori, K. Siratori, Electronic Conduction in Oxides, 2nd ed., Springer, New York, 2000.
[44] S. Brunauer, P.H. Emmet, E. Teller, Adsorption of gases in multimolecular layers, J. Am. Chem. Soc. 60 (1938) 309–319.
[45] M.M. Dubinin, in: J.F. Danielli, M.D. Rosenberg, D.A. Cadenhead (Eds.), Progress in Surface and Membrane Science, vol. 9, Academic Press, New York, 1975, pp. 1–70.
[46] J. Sánchez-González, A. Macías-García, M.F. Alexandre-Franco, V. Gómez-Serrano, Electrical conductivity of carbon blacks under compression, Carbon 43 (2005) 741–747.
[47] S. Mrozowski, Studies of carbon powders under compression, in: Proceedings of the 3rd Biennal Carbon Conference, Pergamon Press, Buffalo, 1957, p. 495.
[48] Y. Ji, Y. Jiang, Increasing the electrical conductivity of poly(vinylidene fluoride) by KrF excimer laser irradiation, Appl. Phys. Lett. 89 (2006) 221103.
[49] S. Torquato, M.D. Rintoul, Effect of the interface on the properties of composite media, Phys. Rev. Lett. 75 (1995) 4067–4070.
[50] W.D. Callister, Materials Science and Engineering. An Introduction, John Wiley & Sons, New York, 2007.
[51] W.W. Smeltzer, R. McIntosh, The effect of physical adsorption on the electrical resistance of active carbon, Can. J. Chem. 31 (1953) 1239–1251.
[52] S.S. Barton, J.E. Koresh, A study of the surface oxides on carbon cloth by electrical conductivity, Carbon 22 (1984) 481–485.
[53] D. Pantea, H. Darmstadt, S. Kaliaguine, L. Sümmchen, C. Roy, Electrical conductivity of thermal carbon blacks. Influence of surface chemistry, Carbon 39 (2001) 1147–1158.
[54] D. Pantea, H. Darmstadt, S. Kaliaguine, C. Roy, Electrical conductivity of conductive carbon blacks: influence of surface chemistry and topology, Appl. Surf. Sci. 217 (2003) 181–193.
[55] D. Pantea, H. Darmstadt, S. Kaliaguine, C. Roy, Heat-treatment of carbon blacks obtained by pyrolysis of used tires. Effect on the surface chemistry, porosity and electrical conductivity, J. Anal. Appl. Pyrolysis 67 (2003) 55–76.
[56] J.G. Hernández, I. Hernández-Calderón, C.A. Luengo, R. Tsu, Microscopic structure and electrical properties of heat treated coals and eucalyptus charcoal, Carbon 20 (1982) 201–205.
[57] F.G. Emmerich, J.C. de Sousa, I.L. Torriani, C.A. Luengo, Applications of a granular model and percolation theory to the electrical resistivity of heat treated endocarp of babassu nut, Carbon 25 (1987) 417–424.
[58] V. Gómez-Serrano, J. Pastor-Villegas, C.J. Durán-Valle, Heat treatment of rockrose char in air. Effect on surface chemistry and porous structure, Carbon 34 (1996) 533–538.
[59] M. Ruíz-Fernández, M. Alexandre-Franco, C. Fernández-González, V. Gómez-Serrano, Development of activated carbon from vine shoots by physical and chemical activation methods. Some insight into activation mechanisms, Adsorption 17 (2011) 621–629.
[60] N.F. Mott, E.A. Davis, Electronic Processes in Non-Crystalline Materials, Clarendon Press, Oxford, 1979.
[61] M. Vogel, O. Stenzel, R. Petrich, G. Schaarschmidt, W. Scharff, The position of the fundamental absorption edge and activation energies for thermally activated electrical conductivity in amorphous carbon layers, Thin Solid Films 227 (1993) 74–89.
[62] H.T. Pinnick, Proceedings of the First Conference on Carbon, American Carbon Society, New York (1956), p. 3–11.
[63] Y.-R. Rhim, D. Zhang, D. Howard Fairbrother, K.A. Wepasnick, K.J. Livi, R. J. Bodnar, D.C. Nagle, Changes in electrical and microstructural properties of microcrystalline cellulose as function of carbonization temperature, Carbon 48 (2010) 1012–1024.

[64] H. Fritzsche, Optical and electrical energy gaps in amorphous semiconductors, J. Non-Crystal. Solids 6 (1971) 49–71.
[65] S. Mrozowski, Semiconductivity and diamagnetism of polycrystalline graphite and condensed ring systems, Phys. Rev. 85 (1952) 609–620.
[66] E.A. Kmetko, Infrared absorption and intrinsic semiconductivity of condensed aromatic systems, Phys. Rev. 82 (1951) 456–457.
[67] B.D. McMichael, E.A. Kmetko, S. Mrozowski, An aromatic detector for the infrared, J. Opt. Soc. Am. 44 (1954) 26–30.
[68] D.E. Weiss, in: S. Mrozowski, M.L. Studebaker, P.L. Walter Jr. (Eds.), Proceedings of the Fifth Carbon Conference, Pergamon, New York, 1962, vol. 1, p. 65.
[69] P.L. Walters, Proceedings of the Fifth Carbon Conference, Vol. II, Pennsylvania State University, 1961, p. 131.
[70] M. Polovina, B. Babić, B. Kaluderović, A. Dekanski, Surface characterization of oxidized activated carbon cloth, Carbon 35 (1997) 1047–1052.
[71] C.A. Dimitriadis, N.A. Hastas, N. Vouroutzis, S. Logothetidis, Y. Panayiotatos, Microstructure and its effect on the conductivity of magnetron sputtered carbon thin films, J. Appl. Phys. 89 (2001) 7954–7959.
[72] R.S. Rao, A.B. Walters, M.A. Vannice, Influence of crystallite size on acetone hydrogenation on copper catalysts, J. Phys. Chem. B 109 (2005) 2086–2092.
[73] K.L. López-Maldonado, P. de la Presa, M.A. de la Rubia, P. Crespo, J. de Frutos, A. Hernando, J.A. Matutes Aquino, J.T. Elizalde Galindo, Effects of grain boundary width and crystallite size on conductivity and magnetic properties of magnetite nanoparticles, J. Nanopart. Res. 16 (2014) 2482.
[74] S.L. Patil, M.A. Chougule, S.G. Pawar, B.T. Raut, S. Sen, V.B. Patil, New process for synthesis of ZnO thin films: microstructural, optical and electrical characterization, J. Alloys Compd. 509 (2011) 10055–10061.
[75] N. Ponpandian, A. Narayanasamy, Influence of grain size on the electrical properties of nanocrystalline zinc ferrite, J. Appl. Phys. 92 (2002) 2770–2778.
[76] K. Pomoni, M.V. Sofianou, T. Georgakopoulos, N. Boukos, C. Trapalis, Electrical conductivity studies of anatase TiO_2 with dominant highly reactive {001} facets, J. Alloys Compd. 548 (2013) 194–200.
[77] K. Pomoni, A. Vomvas, C. Trapalis, Dark conductivity and transient photoconductivity of nanocrystalline undoped and N-doped TiO_2 sol–gel thin films, Thin Solid Films 516 (2008) 1271–1278.
[78] F.F. Vol'kenstein, Electronic Processes on Semiconductor Surfaces at Chemisorption, Nauka, Moscow, 1987.
[79] M.C. Horrillo, P. Serrini, J. Santos, L. Manes, Influence of the deposition conditions of SnO_2 thin films by reactive sputtering on the sensitivity to urban pollutants, Sens. Actuators B 45 (1997) 193–198.
[80] T. Prasada-Rao, M.C. Santhoshkumar, Effect of thickness on structural, optical and electrical properties of nanostructured ZnO thin films by spray pyrolysis, Appl. Surf. Sci. 255 (2009) 4579–4584.
[81] B.M. Arghiropoulos, S.J. Teichner, Electrical conductivity of pure and doped zinc oxides, catalysts of the hydrogenation of ethylene. I. Activation of the catalyst and adsorption of oxygen on pure zinc oxide, J. Catal. 3 (1964) 477–487.
[82] A. Cimino, E. Molinari, F. Cramarossa, Oxygen chemisorption and surface p-type behavior of zinc oxide powders, J. Catal. 2 (1963) 315–323.
[83] M. Căldăraru, D. Sprînceana, V.T. Popa, N.I. Ionescu, Surface dynamics in tin dioxide-containing catalysts II. Competition between water and oxygen adsorption on polycrystalline tin dioxide, Sens. Actuators B 30 (1996) 35–41.
[84] M.G. Hutchins, O. Abu-Alkhair, M.M. El-Nahass, K. Abdel-Hady, Electrical conduction mechanisms in thermally evaporated tungsten trioxide (WO_3) thin films, J. Phys. Condens. Matter 18 (2006) 9987–9997.
[85] Z. Chen, C. Lu, Humidity sensors: a review of materials and mechanisms, Sensor Lett. 3 (2005) 274–295.
[86] B. Tryba, A.W. Morawski, M. Inagaki, Application of TiO_2-mounted activated carbon to the removal of phenol from water, Appl. Catal. B 41 (2003) 427–433.
[87] G. Liu, C. Han, M. Peláez, D. Zhu, S. Liao, V. Likodimos, N. Ioannidis, A.G. Kontos, P. Falaras, P.S.M. Dunlop, J.A. Byrne, D.D. Dionysiou, Synthesis, characterization and photocatalytic evaluation of visible light activated C-doped TiO_2 nanoparticles, Nanotechnology 23 (2012) 294003.
[88] D. Huang, Y. Miyamoto, T. Matsumoto, T. Tojo, T. Fan, J. Ding, Q. Guo, D. Zhang, Preparation and characterization of high-surface-area TiO_2/activated carbon by low-temperature impregnation, Sep. Purif. Technol. 78 (2011) 9–15.
[89] Y. Liu, S. Yang, J. Hong, C. Sun, Low-temperature preparation and microwave photocatalytic activity study of TiO_2-mounted activated carbon, J. Hazard. Mater. 142 (2007) 208–215.
[90] J. Matos, A. García, L. Zhao, M.M. Titirici, Solvothermal carbon-doped TiO_2 photocatalyst for the enhanced methylene blue degradation under visible light, Appl. Catal. A 390 (2010) 175–182.
[91] A.W. Meyer, H. Neldel, Z. Tech. Phys. 18 (1937) 588–593.